Influence of vehicle back shape on wheel-vehicle aerodynamic interactions: a model study

Di Bao, Jacques Borée, Christophe Sicot, Côme Roebroeck

Di Bao, Jacques Borée, Christophe Sicot, Côme Roebroeck. Influence of vehicle back shape on wheel-vehicle aerodynamic interactions: a model study. Experiments in Fluids, 2024, 65 (4), pp.50. 10.1007/s00348-024-03790-4 . hal-04516352

HAL Id: hal-04516352
https://hal.science/hal-04516352v1

Submitted on 22 Mar 2024

Noname manuscript No.
(will be inserted by the editor)

Influence of vehicle back shape on wheel-vehicle aerodynamic interactions: a model study

Di Bao[1] · **Jacques Borée** [1] · **Christophe Sicot**[1] · **Côme Roebroeck** [2]

Received: date / Accepted: date

Abstract The influence of vehicle back shape on wheel-vehicle aerodynamic interactions is investigated in a model situation. A pair of D-shaped obstacles is placed under a fast-back or a square-back Windsor body to mimic the blockage of the wheels and to induce near-wake interactions at the base of the body. By varying the distance l between the obstacles and the base of the body, the consequences of near-wake interactions are analyzed for both geometries. For both bodies, when the obstacle-to-base distance is small $l/d < 2.5$ (d is the width of the obstacles), a mean mass transfer from the main body wake to the obstacle wakes is measured which is responsible for a base drag increase of up to 18%. For identical settings of the obstacles, both mass transfer and drag increase are not sensitive to the shape of the model. This observation is analyzed using both experimental and numerical data. On the other hand, the mean wake topology of the fast-back body is found to be much less sensitive to the obstacles compared to the square-back body.

Keywords Automotive aerodynamics · drag · wheels · wake dynamics

1 Introduction

The driving range of ground vehicles at highway speeds is mainly dictated by the aerodynamic drag, which accounts for over 50% of the vehicle's total energy consumption (Schuetz, 2016). The separation regions around a ground vehicle and the interactions between them are direct or indirect sources of aerodynamic drag. Considering the scale of the separation regions, the wheel wakes and the vehicle wake are the dominant ones. Indirect effects of the wheels on the near wake of the main body leading to a decrease in the base pressure have a very detrimental impact on the aerodynamic efficiency of a vehicle. To give some figures, the wheels themselves and their interactions with the main body are responsible for more than 25% of the aerodynamic drag (Wickern *et al.*, 1997).

The signatures of wheel-vehicle interactions have been observed in previous studies by adding fixed or rotating wheels to a vehicle (Wickern *et al.*, 1997; Wang, 2019; Pavia, 2019), by actuating the wheels (Elofsson & Bannister, 2002; Pavia & Passmore, 2017; Wang *et al.*, 2019), or by varying the tire/rim shape (Landström *et al.*, 2009, 2011; Brandt *et al.*, 2019; Josefsson *et al.*, 2022). However, to the authors' knowledge, the underlying flow mechanisms concerning the coupling between the large-scale wake of a vehicle and the wake of the wheels have only been analyzed recently with the help of an understanding based on simplified vehicle models.

The Ahmed body (Ahmed *et al.*, 1984) and the Windsor body (Le Good & Garry, 2004) are perhaps the most widely used simplified vehicle models. For the square-back version of these two models, the near wake and the drag were found to be very sensitive to flow perturbations. When perturbations are induced in the underflow, the near wake balance and drag were found to be modified. Some examples are: placing obstacles (Barros *et al.*, 2017; Haffner *et al.*, 2020), changing the pitch angle (Bonnavion & Cadot, 2018; Fan *et al.*, 2022) or varying the underflow momentum (Grandemange *et al.*, 2013*a*; Castelain *et al.*, 2018). Inspired by these sensitivity studies, Bao *et al.* (2022) placed a pair of D-

---

✉ Di Bao
E-mail: di.bao@ensma.fr

[1] Institut PPRIME-UPR 3346, CNRS - ENSMA- Université de Poitiers, 86360 Futuroscope Chasseneuil, France

[2] MFP Michelin, Site de LADOUX, Clermont-Ferrand, France.

shaped obstacles in the underflow of a square-back Windsor body to mimic the effects of the wheels. As soon as the obstacles are placed in the underflow, the vertical wake balance is modified. Moreover, by varying the distance between the obstacles and the base, a mean mass transfer was observed from the main body wake to the wakes of the obstacles. This happens when the distance between the obstacles and the base is smaller than 2.5 times the obstacle width. These two flow mechanisms of wheel-vehicle interactions were further validated in Bao *et al.* (2023) in a more realistic setup with the use of rotating wheels.

These previous results have enriched our understanding of the wheel-vehicle interaction problem and opened new possibilities to further control the interactions. However, only a square-back model was considered in Bao *et al.* (2022, 2023) while it is well-known that different vehicles have different sensitivities to the modifications on wheels (Wittmeier *et al.*, 2013; Hobeika *et al.*, 2013). Therefore, there is a real need for examining the wheel-vehicle interactions on different vehicle shapes.

In the present work, we examine the wheel-vehicle interactions on two different bluff body shapes using the approach of Bao *et al.* (2022), by placing a pair of D-shaped obstacles in the underflow. In addition to a square-back body, our choice is a $\alpha = 20°$ fast-back with a highly 3-D near wake. A full description and review of the general flow features of the fast-back are not given here for brevity but can be found for example in Zhang *et al.* (2015). Our aim is to show what are the differences and similarities of the near-wake interactions between the two bluff bodies. The final aim is to generalize the conclusions of wheel-vehicle interactions found in Bao *et al.* (2022) and in Bao (2023). A detailed experimental investigation is presented first in §2, followed by a supplementary numerical investigation in §3. Finally, in §4, discussion and concluding remarks are proposed.

2 Wind tunnel experiments

2.1 Experimental setup

2.1.1 Wind tunnel facility and model geometry

The experiments are performed in the S620 closed-loop wind tunnel of ISAE-ENSMA having a 5 m long test section with a 2.4 × 2.6 m^2 rectangular cross-section. At most operating conditions, the turbulence intensity of the incoming flow is of the order of 0.3 % and the spatial inhomogeneity is lower than 0.5 %. The arrangement inside the test section is detailed in Bao (2023). Briefly, a raised floor composed of an elliptical leading edge, a flat plate and a downstream flap is used to control the ground boundary layer. The displacement thickness of this boundary layer in front of the model is around 2% of the ground clearance of the model. The streamwise pressure gradient above the floor is compensated by the flap located at the trailing edge of the floor, which is regulated to $\alpha = 2°$. The blockage ratio above the floor caused by the model is 2.4 %, which makes blockage correction unnecessary.

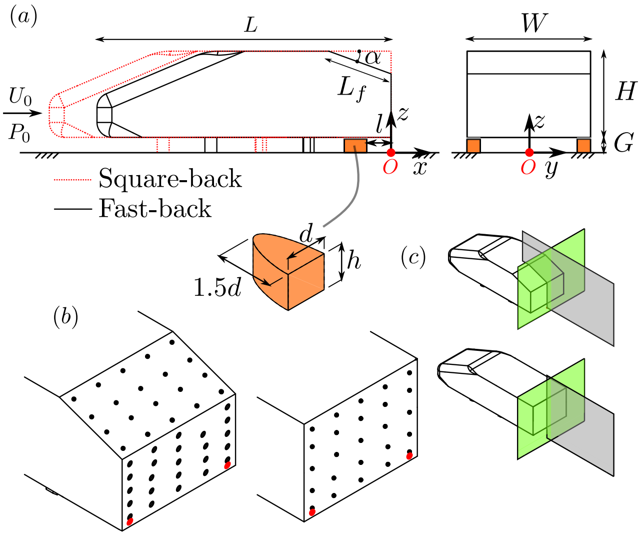

Fig. 1 Experimental set-up. (*a*) Arrangement of the model above a raised floor, a detailed picture of the obstacle is inserted. (*b*) Locations of pressure taps on the base surfaces. (*c*) Positions of the PIV (particle image velocimetry) fields of view.

As shown in figure 1(*a*), two Windsor bodies (Le Good & Garry, 2004) are considered for the present paper. The fast-back (square-back) Windsor body with height H = 0.289 m, width W = 0.389 m and length L = 0.986 m (1.147 m) is placed on the raised floor with a ground clearance of $G = 50$ mm. The length of the slanted base L_f having an angle of $\alpha = 20°$ is 0.222 m.

Unless otherwise stated, all the results presented are collected under a free-stream velocity U_0 = 25 m s^{-1}, corresponding to a height-based Reynolds number $Re_H = U_0H/\nu = 4.8 \times 10^5$, where ν is the kinematic viscosity of the air at operating temperature. The origin O of the coordinate system (x, y, z) (shown in figure 1*a* behind the body) is located at the intersection point of the floor, the vertical rear surface (the vertical base) and the symmetry plane of the bodies, with x, y and z defined respectively along the streamwise, spanwise and floor-normal directions. Under this system, the velocity vector is decomposed into $u = (u_x, u_y, u_z)$. Unless otherwise stated, all physical quantities are normalized by any appropriate combination of the model height H, the free-stream velocity U_0 and the air density ρ during the measurements. For convenience, the normalized velocity vector is denoted by lowercase letters, i.e. $u = (u_x, u_y, u_z) = (U_x/U_0, U_y/U_0, U_z/U_0)$. The Reynolds decomposition is employed to decompose a quantity $\mathscr{X}$ into

$\mathscr{X} = \overline{\mathscr{X}} + \mathscr{X}'$, where $\overline{\mathscr{X}}$ and $\mathscr{X}'$ respectively denote its time-averaged and fluctuation components.

2.1.2 *Underflow perturbations*

In order to perturb the body wake as well as its drag, a similar approach as in Wang (2019) and in Bao *et al.* (2022) is used with a pair of obstacles placed upstream the vertical base surface of the bodies (at $x \leq 0$), between the underside of the bodies and the floor (see figure 1a). The obstacles are of half-elliptic shape. Their length equal to one and a half times the width d. The width and height of the obstacles are d/H = 0.19 and $h/H = 0.17$, respectively. The height generates two $\delta = G - h$ =1.5 mm gaps between the body and the obstacles which are carefully filled with high-density foams. This disables the measurements of the aerodynamic force acting on the model. However, the main focus of the present work is the modifications in the wake of the bodies and therefore the base pressure is sufficient for quantifying the main effects of the obstacles.

The obstacle pair is always placed symmetric to the symmetry plane of the model, with its rear surface parallel to the vertical base surface of the body and its left/right side tangents to the left/right side of the body. The degree of freedom of the pair in the streamwise direction is fixed by the obstacle-to-base distance l (see figure 1a), which is defined as the streamwise distance from the base of the obstacles to the vertical base surface of the body. The parameter l ranges from 0 d (flush-mounted to the base) to 5 d.

2.1.3 *Pressure measurements*

Two different pressure measurement systems are used to perform surface pressure measurements. The first one used for time-averaged and long-timescale measurements includes a 64-channel ESP-DTC pressure scanner linked to 1 mm diameter pressure taps located around the model by 78 cm long vinyl tubes. As shown in figure 1(b), 45 pressure taps are used for the fast-back and are located on the slanted and vertical base surfaces. For the square-back, 25 pressure taps are used. The accuracy of the scanner lies respectively below ±1.5 Pa. Acquisitions from the scanners are conducted at a sampling rate of 100 Hz.

The second system dedicated to time-resolved measurements contains two differential pressure sensors (SensorTechnics HCLA 02X5DB) connected to the pressure taps located on the base near the obstacles. The measurements are a posteriori calibrated and corrected to compensate for the pressure distortions induced by the tubings so that the frequency response of the system is flat on the whole frequency range considered in the present study. A sampling frequency of 2000 Hz is used for this system with an accuracy of ±0.7 Pa.

The pressure coefficient C_p is classically defined as:

$$C_p = \frac{p - p_0}{0.5\rho U_0^2}, \qquad (1)$$

where the reference static pressure p_0 is obtained at $x/H = -1.6$ from a Pitot tube installed at the ceiling of the test section. For all the cases gathered, the duration of the pressure measurements is 300 s. For the unperturbed square-back case presenting lateral bi-modal behavior on a long-timescale of the order of $O(10^3 H/U_0)$ (Grandemange *et al.*, 2013b), this measurement duration is not sufficient to obtain complete statistical convergence. Nevertheless, this time window is chosen as a compromise between a reasonable duration of the experimental campaign and a satisfactory convergence of the mean base pressure. For several mean base pressure values of the unperturbed square-back case obtained from all measurement days (the campaign spans several weeks), the standard deviation of the mean base pressure values is below 2 % of their average value. In order to further reduce the error due to the daily variations of the pressure measurement, the obtained base pressure values of the perturbed cases are expressed relative to the value of the unperturbed case of the same measurement day.

For the square-back configuration, the pressure drag from the base is quantified by the base drag coefficient:

$$C_B = -\frac{\int_B C_p ds}{HW}, \qquad (2)$$

where B represents the base surface. For the fast-back configuration, the base drag coefficient is:

$$C_B = -\frac{sin(20^\circ)\int_{BS} C_p ds + \int_{BV} C_p ds}{HW}. \qquad (3)$$

Separate mean base pressure can be defined for the slanted base (BS) and the vertical base (BV) with:

$$C_{pbS} = \frac{\int_{BS} C_p ds}{\int_{BS} ds}, C_{pbV} = \frac{\int_{BV} C_p ds}{\int_{BV} ds}. \qquad (4)$$

2.1.4 *Aerodynamic force measurements*

A six-component aerodynamic balance (9129AA Kistler piezoelectric sensors and 5080A charge amplifier) connected to the model is used to quantify the unperturbed cases. Force measurements are performed at a sample rate of 200 Hz. The accuracy of the balance lies below 0.6 % of the full range, representing 1 % in the mean drag force $\overline{F_x}$ and 4 % in the mean lift force $\overline{F_z}$. The force coefficients are defined as:

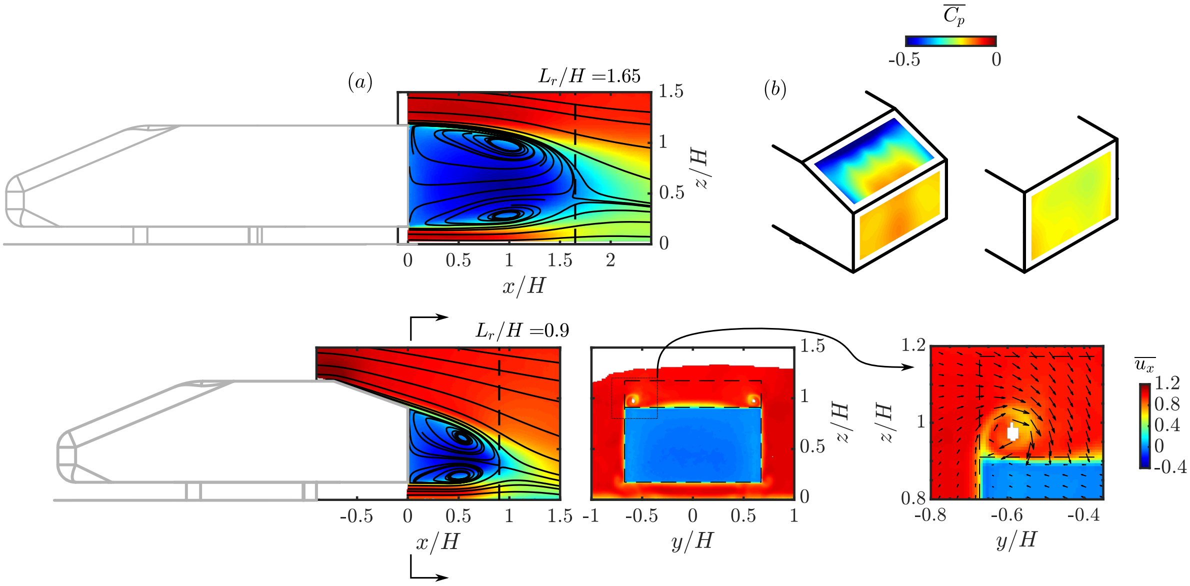

Fig. 2 Baseline flow around the square- and fast-back Windsor bodies. (a) Mean streamwise velocity $\overline{u_x}$ distributions in the symmetry plane of the body ($y/H = 0$, superimposed with mean streamlines) and in the cross-flow plane at $x/H = 0.03$ (for the fast-back). A zoom view is given for the cross-flow plane superimposed by in-plane mean velocity vectors. (b) Mean pressure distributions on the base surfaces of the models.

$$C_i = \frac{F_i}{0.5\rho U_0^2 HW}, \quad i \in \{x, y, z\}. \tag{5}$$

The force measurements are always performed simultaneously with the pressure measurements with the same sampling duration. Therefore the same conclusion regarding the statistical convergence is achieved.

2.1.5 Velocity measurements

The velocity fields in the near wake are measured by a particle image velocimetry (PIV) system. The system consists of a Quantel EverGreen 2 × 200mJ laser and two LaVision Imager LX 16 Mpx cameras. The seeding of the flow is introduced downstream of the raised floor and recirculates through the tunnel closed circuit. Particles with diameter of 1 μm are generated by atomization of mineral oil. Two two-dimensional (2-D) fields of view (FOVs) are considered, as depicted in figure 1(c). The first one located in the symmetry plane of the body ($y/H = 0$) is of two-component (2D2C) set-up, obtaining the streamwise u_x and vertical u_z velocity components. The width (height) of this FOV is 3.2H (1.9H). The second FOV is located in a cross-flow plane in proximity to the base of the body ($x/H = 0.03$). This FOV is of stereoscopic (2D3C) set-up, capturing three velocity components. The width (height) of this FOV is 2.6H (1.4H).

For representative cases, 1200 independent pairs of images are captured from each FOV at a sample rate of 4 Hz, which is satisfactory for statistical convergence of first- and second-order statistics. The image pairs are processed using DaVis 10.1 with a final interrogation window of 32 × 32 pixels for all FOVs. All the processing is performed with an overlap of 50 %. The resulting vector spacing is 0.0091H for the body symmetry plane and 0.0074H for the cross-flow plane. The maximum uncertainty on the instantaneous velocity fields from different FOVs considering an absolute displacement error of 0.1 pixels is estimated to be less than 0.01U_0.

2.2 Results

2.2.1 Baseline flows

The unperturbed baseline cases are now briefly characterized. To this end, the wake flow for both the square- and fast-back configurations is presented in figure 2(a). The mean streamwise velocity $\overline{u_x}$ superimposed with mean streamlines in the symmetry plane $y/H = 0$ is shown. The square-back baseline presents massive flow separation behind the model base, forming a recirculation region having a vertical balanced topology. In figure 2(a), the mean length of the recirculation region is defined by:

$$L_r = max(x)_{\overline{u_x}<0}. \tag{6}$$

On the other hand, the fast-back baseline has a more complex wake topology. From the top surface of the model, we notice a strong flow curvature near the leading edge of the slanted base. Then, the flow is fully attached over the slanted base with no observable separation bubble[1]. At

---

[1] The fast-back part of the vehicle model is manufactured using composite material. Therefore, the top leading edge of the slanted base

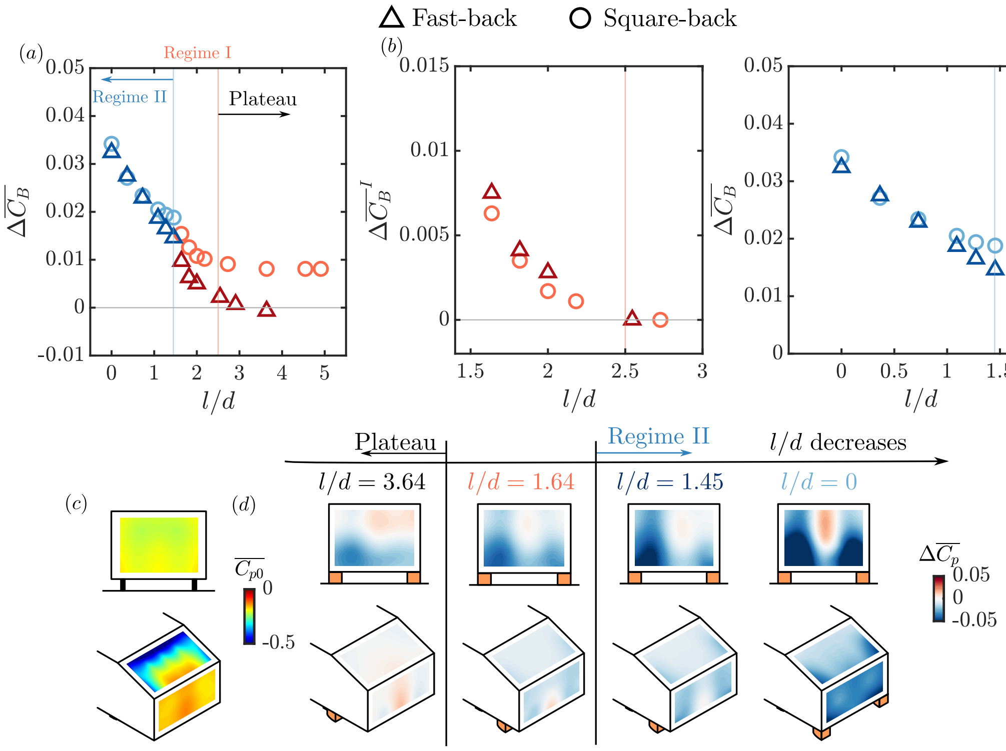

Fig. 3 (a) Base drag variation of the bodies $\Delta\overline{C_B} = \overline{C_B} - \overline{C_{B0}}$ as a function of the obstacle-to-base distance l/d. (b) Comparison of base drag changes in regime I and regime II. (c) Mean base pressure distribution for the baseline cases. (d) Distributions of base pressure differences for different l/d cases with reference to the baseline cases.

the trailing edge of the slanted base, the flow separates and forms a recirculation region extending towards $x/H = 0.9$.

The pressure distributions on the slanted and vertical base surfaces are shown in figure 2(b). The flow curvature at the leading edge of the slanted surface induces a local decrease in pressure. Then, the progressive reduction of the body cross-section results in a pressure recovery before the flow separation and a higher base pressure of $\overline{C_{pbV}} = -0.150$ on the vertical surface compared to $\overline{C_{pb}} = -0.189$ for the square-back. The wake in the cross-flow plane at $x/H = 0.03$ is shown in figure 2(a). Apart from the recirculation region behind the vertical base, the C-pillar vortex pair developed from the two side edges of the slanted base is observed (see also the zoom in figure 2a). It is formed from the separation of the side boundary layers at the two side edges of the slanted base, as indicated by the trace of low-momentum flow inside the streamwise vortex. These structures are responsible for the low-pressure regions measured in figure 2(b) near the two side edges of the slanted base.

The mean aerodynamic coefficients for the baseline cases are summarized in table 1. The base drag and base pressure coefficients will be used in the subsequent section as reference values in order to quantify the effects of the underflow perturbations. The lift coefficient $\overline{C_{z0}}$ for the fast-back model presents a positive value instead of a downforce experienced by the square-back model. This is mainly due to the negative pressure coefficient on the slanted surface.

	$\overline{C_{B0}}$	$\overline{C_{pbS0}}$	$\overline{C_{pbV0}}$	$\overline{C_{x0}}$	$\overline{C_{z0}}$
Fast-back	0.197	-0.331	-0.150	0.219	0.258
Square-back	0.189	-	-	0.226	-0.137

Table 1 Mean aerodynamic coefficients of the baseline cases. From left to right: base drag, base pressure of the slanted and vertical surfaces, total drag, total lift.

2.2.2 Global effects of underflow perturbations

The base drag variation $\Delta\overline{C_B} = \overline{C_B} - \overline{C_{B0}}$ with the relative obstacle-to-base distance l/d is shown in figure 3(a). A major difference between the fast-back and the square-back configurations is noticed. When the obstacles are placed the most upstream of the vertical base surface at the maximum l/d, no obvious change in the base drag is measured for the fast-back configuration. Nevertheless, the trends of these two configurations are very similar. Indeed, moving the obstacles from the most upstream position (maximum l/d) towards the vertical base surface with decreasing l/d, a rapid increase in base drag is noticed from $l/d = 2.5$ to 0. Maxi-

---

is not sharp but the radius of curvature is of order 0.5 mm. This curvature, according to Thacker *et al.* (2012); Rossitto *et al.* (2016), has a fundamental influence on the flow separation over the slanted base.

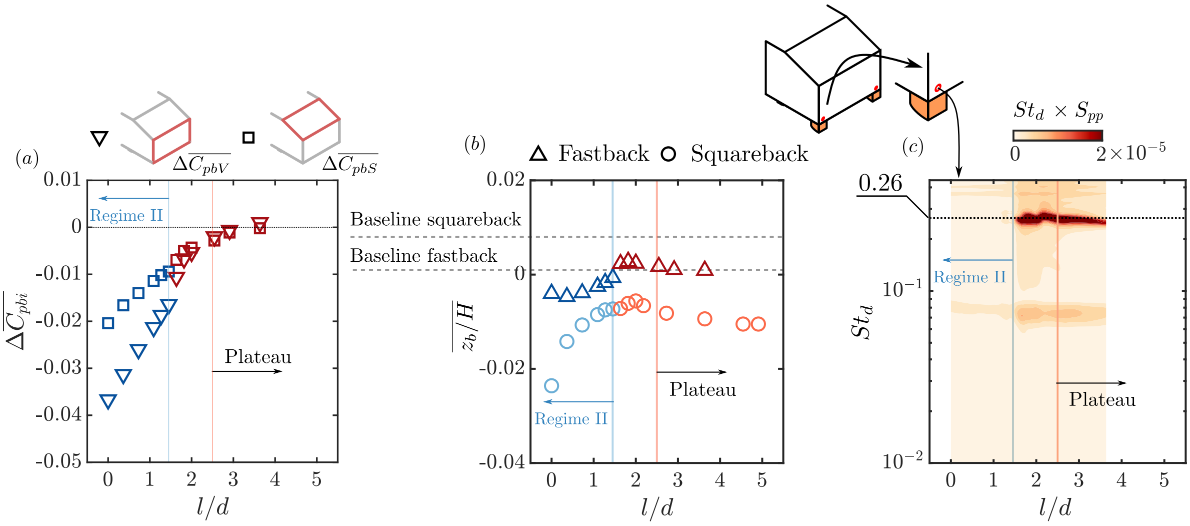

Fig. 4 (*a*) Base pressure variations of the slanted surface and the vertical surface with l/d for the fast-back configuration. (*b*) Evolution of the mean vertical position of the base center-of-pressure (CoP) $\overline{z_b/H}$ with l/d for the two configurations. $\overline{z_b/H}$ is calculated using the vertical base for the fast-back. (*c*) Evolution of the premultiplied spectrum from the pressure sensors (connected to the pressure taps near the obstacles highlighted by red dots in the schematics) with l/d for the fast-back configuration.

mally, we measure a base drag increase of $\Delta\overline{C_B}/\overline{C_{B0}} \approx 16\%$ for the fast-back configuration and 18% for the square-back configuration when the obstacles are flush-mounted to the base ($l/d = 0$).

For the square-back configuration, we observe a clear plateau at $l/d > 2.5$ with a very slight variation of the base drag. However, the cases having l/d values larger than 4 are not tested for the fast-back configuration due to mechanical constraints. Nevertheless, the range $l/d > 2.5$ is named as the plateau for both configurations. Discussion of the detailed measurements will confirm this statement in what follows. By looking at the pressure fluctuations in the wake of the obstacles (will be detailed later in figure 4*c*), two drag-sensitive regimes, regime I and II, are defined for the range $l/d < 2.5$. The l/d ranges for these two regimes are $1.5 < l/d < 2.5$ and $l/d < 1.5$, respectively.

In figure 3(*b*), we further compare the variations of the base drag in regime I and II between the two configurations. In regime II, for obstacles close to the vertical base, we notice that the base drag increase is measured to be very similar. This observation suggests that the flow mechanisms resulting in the base drag increase are the same for the two different back shapes. In regime I, the level of base drag increases from the plateau $\Delta\overline{C_B}^I = \overline{C_B} - \overline{C_B}(l/d = 2.5)$ is also weakly sensitive to the shape of the body.

The mean pressure distributions on the base are now analyzed to better understand how the base drag is modified by the obstacles. In figure 3(*c*) the base pressure distributions for the baseline cases are shown again. With respect to these two cases, the distributions of pressure difference for different l/d cases are presented in figure 3(*d*).

We focus first on the square-back configuration. When the obstacles are placed at $l/d = 3.64$ (plateau), the vertical base pressure gradient is varied indicating a modification of the mean vertical wake balance. With decreasing l/d, the base pressure decreases are mainly located in the vicinity of the obstacles.

For the fast-back configuration, when the obstacle pair is placed at $l/d = 3.64$ (plateau), a slight decrease of pressure at the left- and right-hand sides of the vertical base is compensated by a pressure recovery near the centerline of the vertical base. On the slanted base, the pressure is not measured to be varied. All these features give the observation in figure 3(*a*) with no observable base drag change. With decreasing l/d from the plateau to regime I, a quite homogeneous decrease of pressure is measured both on the vertical base and the slanted base. In regime II with decreasing l/d, a further decrease of base pressure is noticed. On the slanted base, the pressure decrease is primarily located near the bottom trailing edge at the left- and right-hand sides. On the vertical base, an important drop is noticed near the obstacles. The pressure evolution on the base surfaces with l/d is further shown in figure 4(*a*) by the evolution of $\Delta\overline{C_{pbV}} = \overline{C_{pbV}} - \overline{C_{pbV0}}$ (mean pressure change on the vertical base) and $\Delta\overline{C_{pbS}} = \overline{C_{pbS}} - \overline{C_{pbS0}}$ (mean pressure change on the slanted base). On both base surfaces, a decrease in pressure is measured in the drag-sensitive regimes with reducing l/d.

In figure 4(*b*), the vertical asymmetry of the recirculation region is quantified by the vertical position of the base center-of-pressure (CoP):

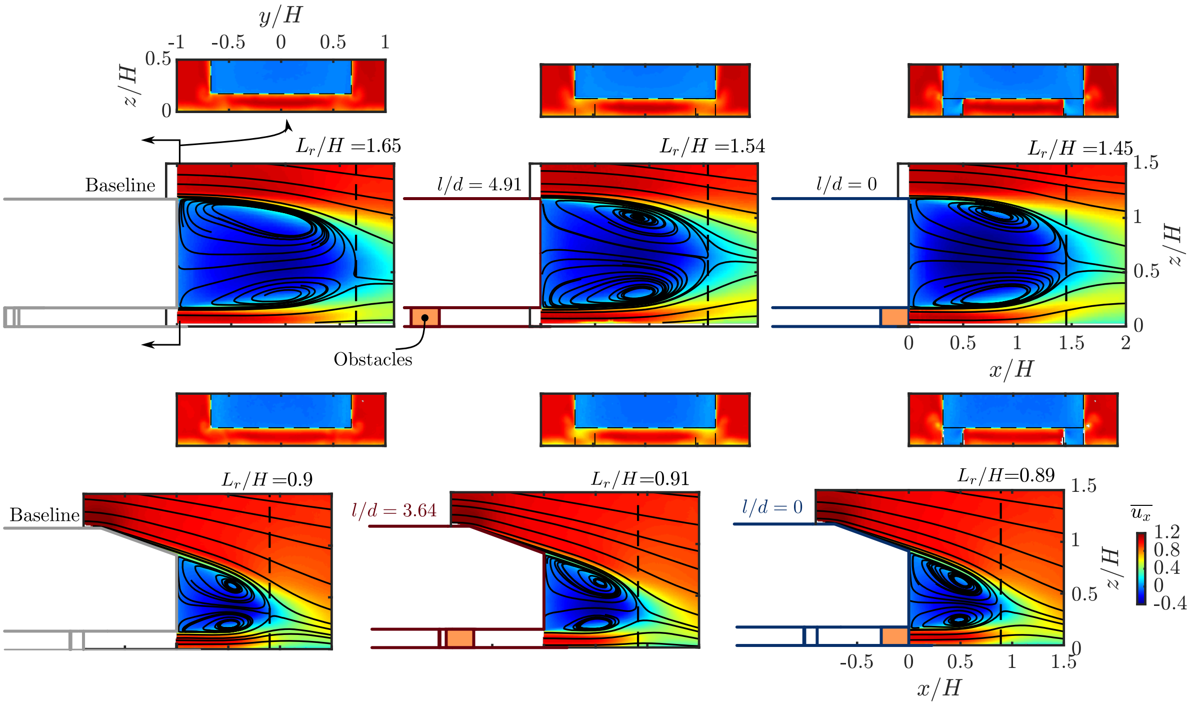

Fig. 5 For the cases without and with obstacles, distributions of mean streamwise velocity $\overline{u_x}$ superimposed by mean streamlines in the symmetry plane of the bodies at $y/H = 0$ and in the cross-flow plane at $x/H = 0.03$.

$$z_b = \frac{\int_{base}(z - z_c)C_p ds}{\int_{base} C_p ds}. \tag{7}$$

where z_c is the vertical coordinate of the center of the base. For the square-back configuration, a large decrease in the mean vertical position of the base CoP $\overline{z_b/H}$ is measured from the baseline to the cases in the plateau. With decreasing l/d, it varies slightly in regime I and decreases tremendously in regime II. On the other hand for the fast-back configuration, the main recirculation region is located downstream of the vertical base. Therefore, $\overline{z_b/H}$ is calculated for the vertical base. From the corresponding baseline, there is no variation in $\overline{z_b/H}$ when the obstacles are located the most upstream of the vertical base surface. With decreasing l/d, a weaker but similar variation in $\overline{z_b/H}$ as the square-back configuration in both regimes is measured. Overall, the vertical wake balance of the fast-back body is less sensitive to the presence of the obstacles in the underflow, especially when they are located relatively far from the base. This is probably the reason for the different $\Delta\overline{C_B}$ values measured in the plateau.

The local flow dynamics near the obstacles are pictured by the premultiplied spectrum from the unsteady pressure sensors (connected to the pressure taps near the obstacles highlighted by red dots in the schematics in figure 4c and figure 1b). The fast-back configuration is considered. In the plateau and regime I, a peak at $St_d = fd/U_0 = 0.26$ (d is the width of the obstacles) is measured. The signature of Karman vortex shedding downstream the obstacles is therefore identified. With decreasing l/d from regime I to II, the peak suddenly disappears at $l/d = 1.5$. This is used as the criterion to separate the regimes. For the square-back body, very similar results were measured (Bao *et al.*, 2022) and are therefore not shown here for brevity. This similarity shows that the obstacle wake dynamical properties and their coupling with the large scale near wake of the body are insensitive to the variation in the body shape.

2.2.3 Global and local wake modifications

In this section, we show how the flow behind the bluff bodies is varied by the presence of the obstacles in the underflow. Mean velocity measurements in the symmetry plane of the model ($y/H = 0$) and in the cross-flow plane ($x/H = 0.03$) are shown in figure 5. We focus first on the measurements in the symmetry plane. For the square-back configuration, as soon as the obstacles are placed in the underflow at $l/d = 4.91$, we observe a change in the vertical mean asymmetry of the recirculating bubble. With reducing l/d, this feature is preserved. On the other hand for the fast-back configuration, we observe no noteworthy change in the recirculating bubble behind the vertical base of the fast-back from the baseline to the $l/d = 3.64$ case. With reducing l/d, the recirculating bubble shows almost no modification. All these observations about the vertical wake asymmetry are in accordance with the examination in figure 4(b) based on the base CoP.

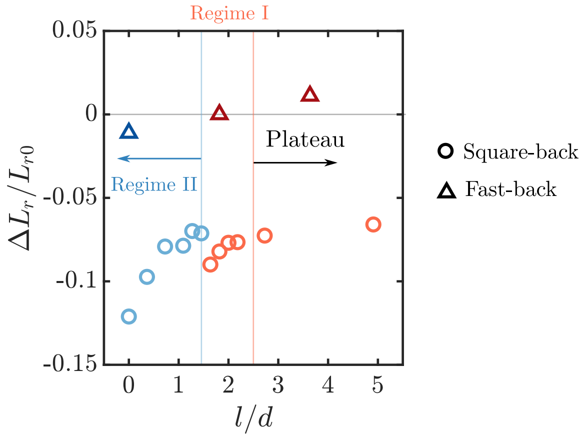

Fig. 6 For both configurations: Evolution of the recirculation length $\Delta L_r/L_{r0} = (L_r - L_{r0})/L_{r0}$ with l/d. L_{r0} is the recirculation length for the baseline cases.

Accompanied by the variations in the vertical asymmetry, we also notice that the length of the recirculation region evolves very differently with l/d for the two configurations. This can be seen in figure 5. To give more details, we show in figure 6 the evolution of $\Delta L_r/L_{r0} = (L_r - L_{r0})/L_{r0}$ with l/d, where L_{r0} represents the recirculation length of the baseline cases. For the square-back configuration, when the obstacles are placed at the maximum l/d, there is a reduction of L_r by $\Delta L_r/L_{r0} \approx 7\%$ from the baseline case. With reducing l/d, L_r decreases gradually in regime I. At the boundary of the regimes ($l/d = 1.5$), there is a sudden change in L_r, which is followed by a rapid decrease in L_r with decreasing l/d in regime II. On the other hand, for all the cases measured for the fast-back configuration, the recirculation length only varies slightly by $\sim 1\%$ relative to the baseline case.

These observations show that the wake topology for the fast-back body is less sensitive to the presence of flow perturbations in the underflow than the square-back body. It is interesting to note that by forcing the bottom shear layer of either fast-back or square-back bluff body, a similar observation can be made by comparing the results in Lorite-Díez *et al.* (2020) and Zhang *et al.* (2018). In Lorite-Díez *et al.* (2020), steady blowing parallel to the streamwise direction was applied along the bottom trailing edge of a square-back Ahmed body. It was shown that even at very small blowing flow rate $C_q = U_b S_b/(U_0 H W) < 0.02$ (U_b and S_b represents, respectively, blowing velocity and surface size), the development of the bottom shear layer is fundamentally changed which impacts the mean vertical balance of the wake and the base pressure. On the other hand, similar steady blowing parallel to the streamwise direction was applied along the bottom trailing edge of a fast-back Ahmed body (Zhang *et al.*, 2018). Although the flow rate C_q is two orders of magnitude higher than in Lorite-Díez *et al.* (2020), the drag is only varied maximally by $\sim 2\%$.

The large-scale recirculation regions of the two configurations are influenced differently by the presence of the obstacles in the underflow. Nevertheless, in the cross-flow plane shown in figure 5, we observe similarities between the two configurations in the region under the main body wake. When the obstacles are placed the most upstream of the vertical base surface, a slight reduction in flow momentum is observed in the wake of the obstacles for both configurations. With decreasing l/d, the flow momentum is further reduced. When the obstacles are flush mounted to the base ($l/d = 0$), the main body wake and the obstacle wake are found to be merged with no mean shear between them. A finer examination of this region downstream of the obstacles is investigated in figure 7(a). For both configurations, with decreasing l/d, the gradual reduction in flow momentum is visualized. By plotting the mean streamwise velocity $\overline{u_x}$ profiles along the centerline of the obstacle in figure 7(b) for all the available cases, a gradual reduction in mean shear between the main body wake and the obstacle wake is noticed for both configurations. In regime II, no mean shear is found between the main body wake and the obstacle wake, indicating that the wakes are merged.

By looking at the in-plane mean vectors shown in figure 7(a), the mean flow topology downstream of the obstacle is very similar between the two configurations. For the cases $l/d = 0$, a mean mass transfer from the main body wake to the obstacle wake is observed for both configurations. Furthermore, in figure 7(c), the strength of the mean mass transfer is quantified by space-averaging the mean vertical velocity $\overline{u_z}$ across the surface of mass exchange having the same width as the obstacles. It is shown that the mean mass transfer is significant in regime II having a magnitude of $\sim 20\%$ of the free-stream velocity. In regime I, the mass transfer also exists but is of a smaller strength. The strength of the mean mass transfer is not found to be sensitive to the shape of the body as can be seen by comparing the $\langle \overline{u_z} \rangle$ evolution between the two configurations.

3 Numerical simulations for the square-back configuration

In this section, numerical simulations are conducted using commercial code Star-ccm+. The simulation guidelines provided in Page & Walle (2022), which are specifically designed for the present square-back geometry, are carefully followed. The objective is not to try to obtain a quantitative agreement with the experiments but to provide more physical analysis and understanding of the 3-D flow for regime II associated with wake merging.

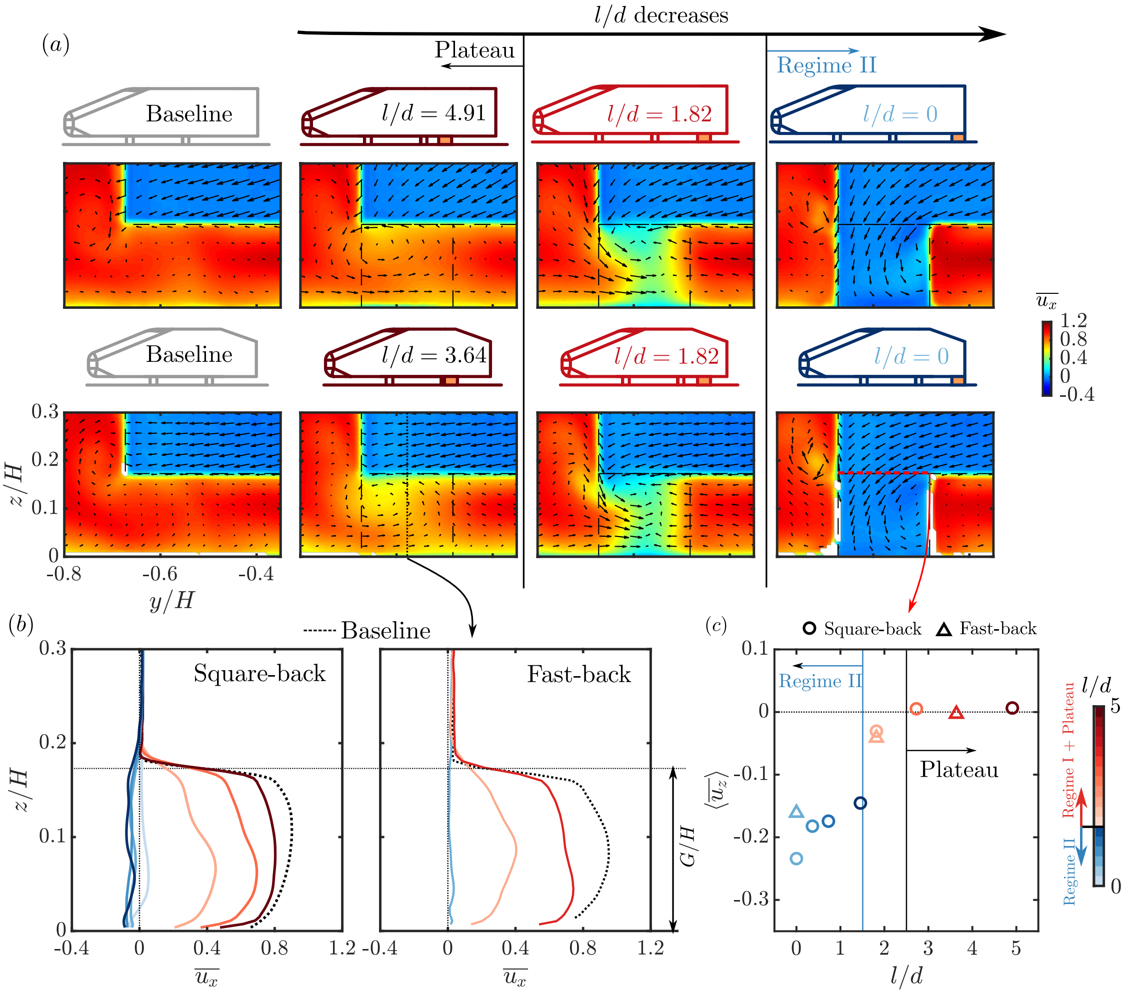

Fig. 7 For both configurations: (a) Local distributions of the mean streamwise velocity $\overline{u_x}$ behind the left-hand obstacle in the cross-flow plane at $x/H = 0.03$. (b) $\overline{u_x}$ profiles along the centerline of the obstacle. (c) Space-averaged mean vertical velocity $\langle \overline{u_z} \rangle$ across the width of the left obstacle at the height of the ground clearance.

3.1 Numerical setup

The numerical setup is now briefly described. A finer description can be found in Bao (2023). The square-back Windsor body is placed inside a computation domain as shown in figure 8 with the same ground clearance as the experiments. The computational domain has the same width and height as the region above the raised floor in the test section. The inlet of the domain is at $8H$ in front of the model and the outlet is at $20H$ behind the model. Different boundary conditions are given for the domain surfaces. A uniform velocity profile at 25 m s $^{-1}$ with turbulence intensity of 0.3 % and turbulence length scale of 0.1 m is set for the inlet. The turbulent kinetic energy (k) and rate of dissipation (ε) at the inlet are deduced from these values assuming isotropy and Kolmogorov law. A pressure outlet condition with a gauge pressure of zero is used for the outlet. For the model surface, a no-slip condition is given. The ground is divided into two parts. From the inlet to $1.8H$ in front of the model, a slip boundary condition is given. The rest of the ground is set to a no-slip boundary condition. This boundary condition for the ground is designed in order to give the same boundary layer thickness approaching the model as the experiments (Östh *et al.*, 2014). In addition, the walls of the domain are specified to a slip boundary condition.

The unstructured mesh inside the computational domain is generated using the commercial code Star-ccm+ following the suggestions of Page & Walle (2022). Behind the model, two regions of mesh refinement are considered. For the cases with the presence of the obstacles, care was taken for the mesh with the cell size near the obstacles reduced by 5 times (proper refinement in the wake region is also considered).

The incompressible RANS equations are solved iteratively based on a finite volume discretization with the Reynolds stresses modeled by eddy viscosity model and the two-equation Realizable $k-\varepsilon$ model (Shih *et al.*, 1995). Due to the high Reynolds number of the present study, the wall-

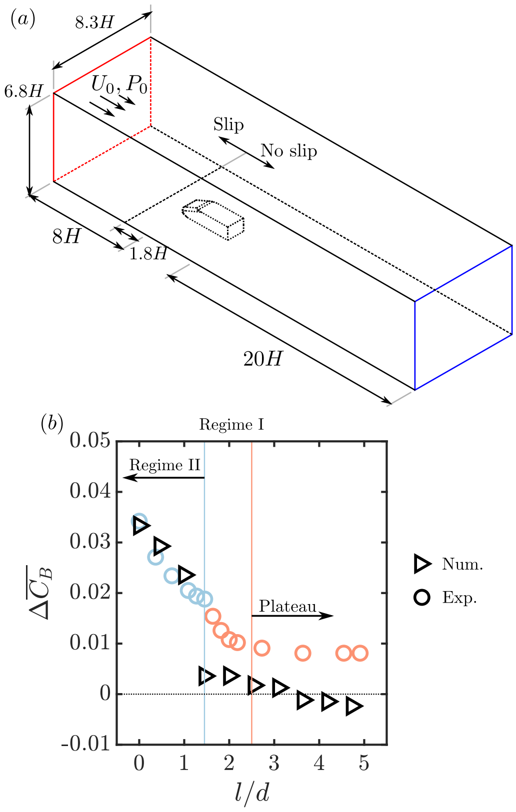

Fig. 8 (*a*) Numerical set-up: Computational domain and boundary conditions, red and blue rectangles represent inlet and outlet, respectively. (*b*) Comparison of the base drag evolution $\Delta\overline{C_B} = \overline{C_B} - \overline{C_{B0}}$ with obstacle-to-base distance l/d between numerical and experimental results.

normal dimension of the first layer cell is set to $y^+ \sim 150$ and the wall functions are used.

The coordinate system and the way to normalize the physical quantities remain the same as in the experiments. The reference velocity U_0 and the reference pressure p_0 are obtained at the location of the pitot tube for the experiments. Based on this numerical setup, special care is taken for the mesh independency, which is detailed in Bao (2023). A total cell number of ~ 5 millions is found for the unperturbed case to be sufficient.

3.2 Results

In figure 8(*b*), the base drag variation $\Delta\overline{C_B} = \overline{C_B} - \overline{C_{B0}}$ of the model with the distance from the obstacles to the base l/d is shown for the simulations and the corresponding experiments. In the plateau, we note that the simulations fail to reproduce the base drag increase of 5 %. From the plateau with decreasing l/d, in regime I the drag sensitivity to l/d is not observed. This is probably due to the failure of the RANS simulations in modeling the complex wake dynamics of the obstacles and their interactions with the main body wake. However, in regime II, we notice the same level of base drag increase $\Delta\overline{C_B}$ and the drag sensitivity to l/d.

Further comparison between the numerical and experimental results, not shown here for brevity, shows that the modifications of the wake balance and obstacle-vehicle interactions in plateau or regime I regions cannot be predicted. However, the near-wake interaction features are quantitatively captured in the strong interaction regime II when the wakes are merged. Specifically, the strength and distribution of the mean mass transfer are quantitively captured. The use of simple eddy-viscosity turbulent models, therefore, permits to obtain further insights into the near-wake interactions in this situation.

We focus, in what follows, on the flush-mounted case ($l/d = 0$, regime II). This case is abbreviated as the case with obstacles. First of all, we focus on the driving factor of the mean mass transfer. A mean streamline from the interaction interface (at $z/H = G/H$, see figure 9*a*) is issued to both forward and backward directions. The evolution of the total pressure coefficient $\overline{C_{pT}}$ along this streamline is plotted in figure 9(a). At any location of the streamline, the value of L_s represents the length of the streamline from the location to the source seed at the interaction interface (marked by the red point in the inserted pictures of figure 9*a*). The sign of L_s denotes the integration direction of the streamline, with a positive (negative) sign representing the forward (backward) direction along the streamline. It is noticed that inside the recirculation region of the main body near the interaction interface ($L_s/H = 0$), $\overline{C_{pT}}$ is relatively conserved. For a part of the streamline shown at the right-hand side of figure 9(a), the total pressure is only varied maximally by $\sim 2\%$ of the dynamic pressure $0.5\rho U_0^2$. Accordingly, along this part of the streamline, $\overline{C_{pT}} = \overline{C_p} + \overline{u}^2$ ($\overline{u}$ is the normalized velocity modulus) is approximately constant. This means that locally the mean mass exchange is mainly driven by the pressure difference between the obstacle wakes and the recirculation region of the body.

In figure 9(b), the mean pressure distributions in the symmetry plane of the model ($y/H = 0$) and in the half-ground-clearance plane ($z/H = 0.09$) are shown. Downstream of the vertical base surface of the main body, a pressure increase is observed between $x/H = 1$ and 2 near the end of the recirculation region. The low-pressure region inside the main body wake influences greatly the pressure distribution in the region under the main body wake. This means that the main body wake sets the background pressure level in the region where the wakes of the obstacles are located. The development of the obstacle wakes further reduces the local pressure level as can be noticed in the horizontal plane behind the obstacles. In the situation considered in this paper, the above pressure relationship suggests that even if the back shape of the body is modified from the square-back to the fast-back, the pressure differ-

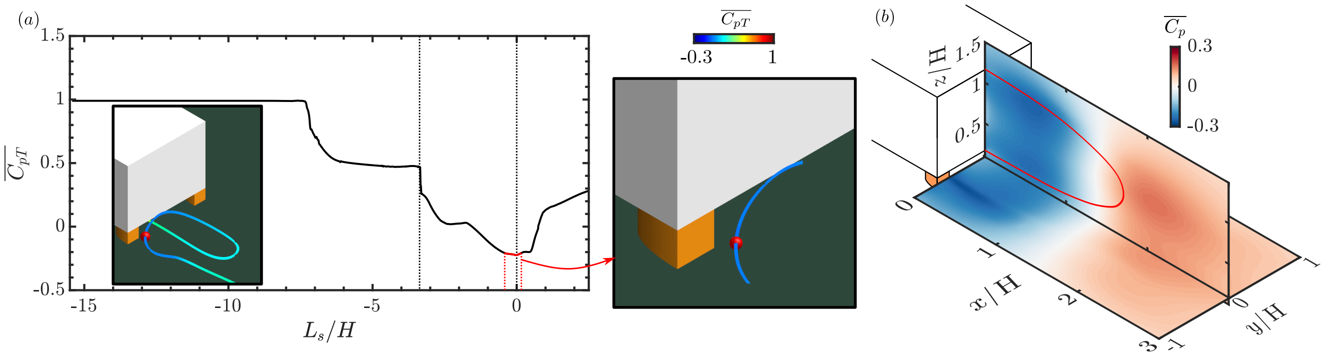

Fig. 9 For the case with obstacles: (a) Total pressure $\overline{C_{pT}}$ evolution along the streamline. L_s is the length of the streamline from the source seed (denoted by the red point in the streamline pictures). A region near the interaction interface with a conserved $\overline{C_{pT}}$ is colored in red. (b) Mean pressure distributions in the symmetry plane of the model ($y/H = 0$) and in the half-ground-clearance plane ($z/H = 0.09$). The red line in the symmetry plane is the mean separatrix.

ence should remain the same. This gives a possible explanation for the insensitivity of the mass exchange phenomenon to body back shape observed in figure 7.

With the 3-D flow data available, the relationship between the mass exchange and base drag increase can be linked together by writing a streamwise momentum balance. To this aim, a control volume is defined in figure 10(a). The volume has a rectangular cuboid shape and a length of $7H$. The length of the volume can be chosen arbitrarily, but here the decision is made so that the base pressure is the main contributor to the surface force acting on the control volume. The upstream surface U of the volume is the base surface. In figure 10(b), the mass flux crossing the bottom surface of the control volume is shown by the distribution of the mean vertical velocity $\overline{u_z}$. At the bottom surface, the mean mass transfer is noted by the negative $\overline{u_z}$ behind the obstacles until $x/H = 1$. The mass exchange at each surface corresponds to a momentum exchange between the control volume and the surrounding flow. This momentum exchange is linked to the base pressure as shown by the streamwise momentum balance:

$$\begin{aligned}&0.5\rho U_0^2 HW\overline{C_B} = \\ &-\int_S \rho\overline{U_x}(\overline{\boldsymbol{U}}\cdot\boldsymbol{dS}) \\ &-\int_D \overline{P}\boldsymbol{dS}\cdot\boldsymbol{x} \\ &-\int_D \rho\overline{U_x'U_x'}\boldsymbol{dS}\cdot\boldsymbol{x}-\int_{L+R}\rho\overline{U_x'U_y'}\boldsymbol{dS}\cdot\boldsymbol{y}-\int_{T+B}\rho\overline{U_x'U_z'}\boldsymbol{dS}\cdot\boldsymbol{z},\end{aligned} \tag{8}$$

where the surfaces T, B, L, R, D and S represent the top, bottom, left-hand side, right-hand side, downstream surfaces and the sum of the aforementioned surfaces, respectively. After all the terms are normalized by $0.5\rho U_0^2 HW$, the three parts at the right-hand side of this equation are denoted by G, F_D, and Tu, respectively. They represent, respectively, the contributions to the base drag of the mean momentum exchange, the downstream pressure modification, and the turbulence. When considering the changes in these terms induced by the obstacles, we observe in figure 10(c) that the change in the momentum exchange ΔG is the dominant contributor to $\Delta\overline{C_B}$ ($\sim 70\%$). This indicates that the enhancement in the momentum exchange between the volume and the surrounding flow is the main contributor to the base drag increase.

Since ΔG is the major contributor to $\Delta\overline{C_B}$, the momentum balance can be written, in a first-order approximation, as:

$$0.5\rho U_0^2 HW\Delta\overline{C_B} \approx -\Delta\int_S \rho\overline{U_x}(\boldsymbol{U}\cdot\boldsymbol{dS}). \tag{9}$$

We then divide the surface of the control volume into two parts, the mass transfer surface BE behind the obstacles with $\overline{u_z} < 0$ and the rest S-BE (see figure 10b). This equation is further written as:

$$0.5\rho U_0^2 HW\Delta\overline{C_B} \approx \Delta\int_{BE} \rho\overline{U_x}(\overline{U_z}dS) - \Delta\int_{S-BE} \rho\overline{U_x}(\boldsymbol{U}\cdot\boldsymbol{dS}). \tag{10}$$

We consider the mass conservation for the control volume, where $\Delta\int_{S-BE}\rho(\boldsymbol{U}\cdot\boldsymbol{dS}) = \Delta\int_{BE}\rho\overline{U_z}dS$. On the surface S-BE, $\overline{U_x}$ is approximately the same order of magnitude as the free-stream velocity U_0 as shown in figure 10(d) by the space-averaged streamwise velocity $\langle\overline{u_x}\rangle$. The equation is therefore transformed into:

$$0.5\rho U_0^2 HW\Delta\overline{C_B} \approx \Delta\int_{BE} \rho(\overline{U_x} - U_0)\overline{U_z}dS. \tag{11}$$

For the unperturbed situation, the flux across BE is negligible. Furthermore, in the perturbed situation, on BE the velocity distribution is mainly vertical, thus $\overline{U_x} - U_0 \approx -U_0$. Therefore:

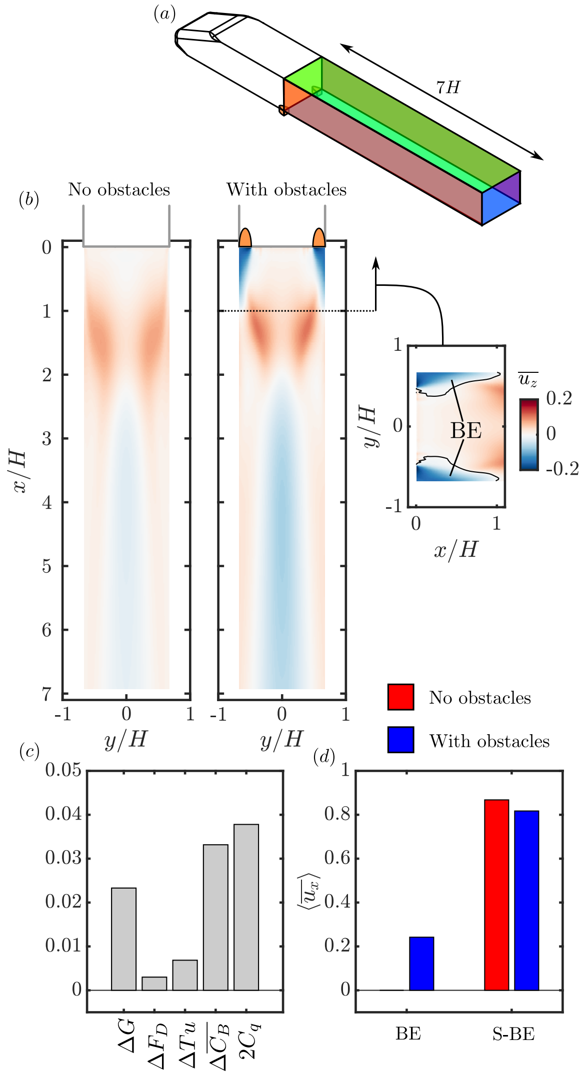

Fig. 10 (a) Definition of a control volume S. (b) For the cases without and with obstacles (flush-mounted to the base): mean mass exchange between the bottom surface of the control volume and the surrounding flow, a subsurface BE is defined with $\overline{u_z} < 0$. (c) The differences of the components in equation 8 between the cases with and without the obstacles. C_q is the mass flow rate of the mean mass transfer from the vehicle wake to the obstacle wakes. (d) Space-averaged streamwise velocity $\langle\overline{u_x}\rangle$ at the surfaces of the control volume.

$$0.5\rho U_0^2 HW\Delta\overline{C_B} \approx -\rho U_0 \int_{BE} \overline{U_z} dS. \tag{12}$$

This means that the continuous "feeding" of the separating region of the body by fluid particles having the upstream longitudinal momentum per unit volume ρU_0 is compensated by an increase in pressure drag. Normalizing each term by $0.5\rho U_0^2 HW$, we finally find:

$$\Delta\overline{C_B} \approx 2\frac{-\int_{BE}\overline{U_z}dS}{HWU_0} = 2C_q. \tag{13}$$

where C_q is the non-dimensional suction flow rate. By comparing $\Delta\overline{C_B}$ and 2Cq, it is shown in figure 10(c) that the simplification of the momentum balance gives a satisfactory result. For low suction flow rates, the same relation $\Delta\overline{C_B} = 2C_q$ was found to govern the base suction experiments in Bearman (1967) for a 2-D D-shaped bluff body and in Hsu *et al.* (2021) for a 3-D Ahmed body. It has been used to analyze this near-wake interaction problem in Bao *et al.* (2022). Therefore, the numerical data helps us to link the local mass exchange with the experimentally measured base drag increase and gives us an order-of-magnitude relationship between them.

4 Discussion and concluding remarks

The influence of vehicle back shape on wheel-vehicle interactions was investigated experimentally in a model situation. By placing a pair of D-shaped obstacles under a square-back or a fast-back Windsor body, similarities and differences between the two bodies in the wheel-vehicle interactions were found and analyzed using both experimental and numerical data.

When looking locally at the flow near the obstacles, we showed that this flow is barely modified by the variation in the back shape. When the distance between the obstacles and the base is smaller than 2.5 times the obstacle width, a mean mass transfer from the body wake to the obstacle wakes is responsible for a base drag increase of up to 18% and is insensitive to the body shape. As a mean mass flux exits the large-scale mean separation bubble downstream of the Windsor body, the mass conservation guarantees that the near wake has to obtain the corresponding mass flux from the high-momentum surrounding flow. In such situations, fluid particles continuously enter the mean recirculating region and therefore lose their longitudinal momentum. Using the 3-D flow data obtained through numerical simulations, a streamwise momentum balance was written to link this momentum exchange and base pressure change. The momentum balance suggests that the same level of mean mass transfer corresponds to the same level of base pressure change. Moreover, we have shown that the mass exchange is mainly driven by the pressure difference between the obstacle wakes and the recirculation region of the body.

When a different vehicle is perturbed using the same obstacles, the global variation in the pressure field of the near wake is driven by the shape of the vehicle but the local pressure difference at the scale of the wheels remains the same. Therefore, the level of mass exchange and the related drag change are expected to be independent on vehicle shape. This was successfully measured experimentally and, as a result, the same pressure drag sensitivity was identified for the two bluff bodies considered in this work.

On the other hand, differences were noticed when looking globally at the wake topology of the main body, which reacts very differently to the presence of the obstacles. Specifically, the vertical wake equilibrium and the recirculation length for the fast-back body were found to be much less sensitive to the obstacles compared to the square-back body.

The present work extended our understanding of multi-scale flow separation situations. The mean mass transfer highlighted in this paper is expected to be a general feature of these flows. As the drag reduction of automotives is concerned, this work provides a framework for further investigating the effects of wheel settings (design, distance to the base, ...) for different vehicle shapes.

Acknowledgements

The authors would like to warmly thank M. Grandemange from MFP Michelin and Y.Haffner from CSTB for insightful discussions, J.-M. Breux for invaluable support during the experiments, as well as F. Paillé, P. Braud and R. Bellanger for technical assistance.

Declarations

Ethical approval. Not Applicable.

Competing interests. The authors report no conflict of interest.

Authors' contributions. D. B.: Conceptualization, Methodology, Software, Data curation, Writing – original draft, Visualization. **J. B.**: Conceptualization, Validation, Reviewing and editing, Resources, Supervision, Project administration, Funding acquisition. **C. S.**: Conceptualization, Reviewing and editing, Resources, Supervision, Project administration, Funding acquisition. **C. R.**: Conceptualization, Validation, Resources, Reviewing and editing, Project administration, Funding acquisition.

Funding. The authors are deeply indebted for the support from MFP Michelin and the CPER Feder programme Transport of Région Nouvelle-Aquitaine. D.B. wishes to acknowledge the support from China Scholarship Council (CSC No. 201806260262).

Availability of data and materials. The authors do not have permission to share data.

References

AHMED, S.R., RAMM, G. & FALTIN, G. 1984 Some salient features of the time-averaged ground vehicle wake. *Tech. Rep.* 840300. Society of Automotive Engineers, Inc.

BAO, D. 2023 Wheel-vehicle aerodynamic interactions: consequences for drag. PhD thesis, Chasseneuil-du-Poitou, Ecole Nationale Supérieure de Mécanique et d'Aérotechnique.

BAO, D., BORÉE, J., HAFFNER, Y. & SICOT, C. 2022 Near wake interactions and drag increase regimes for a square-back bluff body. *J. Fluid Mech.* **936**, A2.

BAO, D., BORÉE, J., SICOT, C. & ROEBROECK, C. 2023 Salient features of wheel-vehicle interactions: consequences on drag. *J. Wind Eng. Ind. Aerodyn.* **236**, 105366.

BARROS, D., BORÉE, J., CADOT, O., SPOHN, A. & NOACK, B.R. 2017 Forcing symmetry exchanges and flow reversals in turbulent wakes. *J. Fluid Mech.* **829**, R1.

BEARMAN, P.W. 1967 The effect of base bleed on the flow behind a two-dimensional model with a blunt trailing edge. *Aeronaut. Q.* **18** (3), 207–224.

BONNAVION, G. & CADOT, O. 2018 Unstable wake dynamics of rectangular flat-backed bluff bodies with inclination and ground proximity. *J. Fluid Mech.* **854**, 196–232.

BRANDT, A., BERG, H., BOLZON, M. & JOSEFSSON, L. 2019 The effects of wheel design on the aerodynamic drag of passenger vehicles. *Tech. Rep.* 2019-01-0662. Society of Automotive Engineers, Inc.

CASTELAIN, T., MICHARD, M., SZMIGIEL, M., CHACATON, D. & JUVÉ, D. 2018 Identification of flow classes in the wake of a simplified truck model depending on the underbody velocity. *J. Wind Eng. Ind. Aerodyn.* **175**, 352–363.

ELOFSSON, P. & BANNISTER, M. 2002 Drag reduction mechanisms due to moving ground and wheel rotation in passenger cars. *Tech. Rep.* 2002-01-0531. Society of Automotive Engineers, Inc.

FAN, Y., PAREZANOVIĆ, V. & CADOT, O. 2022 Wake transitions and steady-instability of an ahmed body in varying flow conditions. *J. Fluid Mech.* **942**.

GRANDEMANGE, M., GOHLKE, M. & CADOT, O. 2013*a* Bi-stability in the turbulent wake past parallelepiped bodies with various aspect ratios and wall effects. *Phys. Fluids* **25** (9), 095103.

GRANDEMANGE, M., GOHLKE, M. & CADOT, O. 2013*b* Turbulent wake past a three-dimensional blunt body. part 1. global modes and bi-stability. *J. Fluid Mech.* **722**, 51.

HAFFNER, Y., BORÉE, J., SPOHN, A. & CASTELAIN, T. 2020 Mechanics of bluff body drag reduction during transient near-wake reversals. *J. Fluid Mech.* **894**, A14.

HOBEIKA, T., SEBBEN, S. & LANDSTROM, C. 2013 Investigation of the influence of tyre geometry on the aerodynamics of passenger cars. *Tech. Rep.* 2013-01-0955. Society of Automotive Engineers, Inc.

HSU, E.C., PASTUR, L., CADOT, O. & PAREZANOVIĆ, V. 2021 A fundamental link between steady asymmetry and separation length in the wake of a 3-d square-back body. *Exp. Fluids* **62** (5).

JOSEFSSON, E., HOBEIKA, T., SEBBEN, S. & URQUHART, M. 2022 Investigation of tyre pattern effect on the aerodynamics of a passenger vehicle. *J. Fluids Eng.* **144** (11), 111209.

LANDSTRÖM, C., LÖFDAHL, L. & WALKER, T. 2009 Detailed flow studies in close proximity of rotating wheels on a passenger car. *Tech. Rep.* 2009-01-0778. Society of Automotive Engineers, Inc.

LANDSTRÖM, C., WALKER, T., CHRISTOFFERSEN, L. & LÖFDAHL, L. 2011 Influences of different front and rear wheel designs on aerodynamic drag of a sedan type passenger car. *Tech. Rep.* 2011-01-0165. Society of Automotive Engineers, Inc.

LE GOOD, G. M. & GARRY, K. P. 2004 On the use of reference models in automotive aerodynamics. *Tech. Rep.* 2004-01-1308. Society of Automotive Engineers, Inc.

LORITE-DÍEZ, M., JIMÉNEZ-GONZÁLEZ, J.I., PASTUR, L., MARTÍNEZ-BAZÁN, C. & CADOT, O. 2020 Experimental analysis of the effect of local base blowing on three-dimensional wake modes. *J. Fluid Mech.* **883**.

ÖSTH, J., NOACK, B. R., KRAJNOVIĆ, S., BARROS, D. & BORÉE,

J. 2014 On the need for a nonlinear subscale turbulence term in pod models as exemplified for a high-reynolds-number flow over an ahmed body. *J. Fluid Mech.* **747**, 518–544.

PAGE, G. J. & WALLE, A. 2022 Towards a standardized assessment of automotive aerodynamic cfd prediction capability-autocfd 2: Windsor body test case summary. *Tech. Rep.* 2022-01-0898. Society of Automotive Engineers, Inc.

PAVIA, G. 2019 Characterisation of the unsteady wake of a square-back road vehicle. PhD thesis, Loughborough University.

PAVIA, G. & PASSMORE, M. 2017 Characterisation of wake bi-stability for a square-back geometry with rotating wheels. In *FKFS Conference*, pp. 93–109. Springer.

ROSSITTO, G., SICOT, C., FERRAND, V., BORÉE, J. & HARAMBAT, F. 2016 Influence of afterbody rounding on the pressure distribution over a fastback vehicle. *Exp. Fluids* **57**, 1–12.

SCHUETZ, T. 2016 *Aerodynamics of road vehicles*. Society of Automotive Engineers, Inc.

SHIH, T.-H., LIOU, W. W., SHABBIR, A., YANG, Z. & ZHU, J. 1995 A new $k-\varepsilon$ eddy viscosity model for high reynolds number turbulent flows. *Comput. fluids* **24** (3), 227–238.

THACKER, A., AUBRUN, S., LEROY, A. & DEVINANT, P. 2012 Effects of suppressing the 3d separation on the rear slant on the flow structures around an ahmed body. *J. Wind Eng. Ind. Aerodyn.* **107**, 237–243.

WANG, S., AVADIAR, T., THOMPSON, M. C. & BURTON, D. 2019 Effect of moving ground on the aerodynamics of a generic automotive model: The drivaer-estate. *J. Wind Eng. Ind. Aerodyn.* **195**, 104000.

WANG, Y. 2019 Experimental study of wheel-vehicle aerodynamic interactions. PhD thesis, Chasseneuil-du-Poitou, Ecole Nationale Supérieure de Mécanique et d'Aérotechnique.

WICKERN, G., ZWICKER, K. & PFADENHAUER, M. 1997 Rotating wheels-their impact on wind tunnel test techniques and on vehicle drag results. *Tech. Rep.* 970133. Society of Automotive Engineers, Inc.

WITTMEIER, F., WIDDECKE, N., WIEDEMANN, J., LINDENER, N. & ARMBRUSTER, R. 2013 Reifenentwicklung unter aerodynamischen aspekten. *ATZ-Automobiltechnische Zeitschrift* **115** (2), 144–150.

ZHANG, B.F., LIU, K., ZHOU, Y., TO, S. & TU, J.Y. 2018 Active drag reduction of a high-drag ahmed body based on steady blowing. *J. Fluid Mech.* **856**, 351–396.

ZHANG, B.F., ZHOU, Y. & TO, S. 2015 Unsteady flow structures around a high-drag ahmed body. *J. Fluid Mech.* **777**, 291–326.